ADVANCED OPTICAL MATERIALS
www.advopticalmat.de

Polarization-Sensitive Photodetectors Based on Directionally Oriented Organic Bulk-Heterojunctions

Aleksandr Perevedentsev, Hadhemi Mejri, Luis A. Ruiz-Preciado, Tomasz Marszalek, Uli Lemmer, Paul W. M. Blom, and Gerardo Hernandez-Sosa**

Polarized spectroscopic photodetection enables numerous applications in diverse areas such as sensing, industrial quality control, and visible light communications. Although organic photodetectors (OPDs) can offer a cost-effective alternative to silicon-based technology—particularly when flexibility and large-area arrays are desired—polarized OPDs are only beginning to receive due research interest. Instead of resorting to external polarization optics, this report presents polarized OPDs based on directionally oriented blends of poly(3-hexylthiophene) (P3HT) and benchmark polymer or nonfullerene acceptors fabricated using a versatile solution-based method. Furthermore, a novel postprocessing scheme based on backfilling and plasma etching is advanced to ameliorate high dark-currents that are otherwise inherent to fibrillar active layers. The resulting polarized P3HT:N2200 OPDs exhibit a broad enhancement across all principal figures of merit compared to reference isotropic devices, including peak responsivities of 70 mA W^{-1} and up to a threefold increase in 3 dB bandwidth to 0.75 MHz under parallel-polarized illumination. Polarization ratios of up to 3.5 are obtained across a spectral range that is determined by the specific donor–acceptor combinations. Finally, as a proof-of-concept demonstration, polarized OPDs are used for photoelasticity analysis of rubber films under tensile deformation, highlighting their potential for existing and emerging applications in advanced optical sensing.

1. Introduction

Among the many applications of organic semiconductors, photodetection has emerged as a major area where the performance of organic photodiodes can compete with, and often surpass, that of conventional silicon-based devices.[1–3] The tunable spectral response of organic semiconductors offers unparalleled versatility in visible to near-infrared optical sensing,[4] while their adaptability to flexible substrates and low-cost solution processing are optimally suited for large-area applications—particularly via the use of inkjet printing to construct complex device arrays.[4,5] Hence, organic photodetectors (OPDs) are increasingly investigated for a diverse palette of applications including wearable biometric sensors,[6] position- and touch detection,[7] lab-on-chip systems,[8] and visible light communication.[4,9]

The capability of detecting and distinguishing linearly polarized light represents the next level of photodetector functionality, yielding higher information density for applications such as polarimetry, (bioinspired) sensing and navigation, and telecommunications.[10–12] To-date there have been several reports of photodetectors based on inorganic materials and metal-halide perovskites where polarized detection is enabled by harnessing anisotropic crystal structure or asymmetric nanowire-type morphologies.[13] While polarized detection with OPDs can be enabled via the use of external or integrated polarization optics,[14] this approach inevitably increases device size, cost and complexity, as well as rejecting a significant fraction of the incident light intensity.

A promising—and currently underexplored—alternative is to exploit the intrinsically anisotropic optoelectronic characteristics of quasi-1D semiconducting polymers, which can be unlocked via directional chain orientation within thin-film active layers. Besides enabling polarized absorption of light without any external polarization optics,[15,16] directional (macro-)molecular orientation of organic semiconductors offers further advantages in terms of device performance. For instance, chain extension and reduced energetic disorder within oriented organic systems lead to significantly improved charge transport[17–20] and may therefore be used to address the remaining bottleneck of the generally limited response speed of

A. Perevedentsev, H. Mejri, L. A. Ruiz-Preciado, U. Lemmer, G. Hernandez-Sosa
Light Technology Institute
Karlsruhe Institute of Technology
Engesser Str. 13, 76131 Karlsruhe, Germany
E-mail: perevedentsev@kit.edu; gerardo.sosa@kit.edu

A. Perevedentsev, H. Mejri, L. A. Ruiz-Preciado, G. Hernandez-Sosa
InnovationLab
Speyerer Str. 4 69 115 Heidelberg, Germany

T. Marszalek, P. W. M. Blom
Max Planck Institute for Polymer Research
Ackermannweg 10, 55128 Mainz, Germany

U. Lemmer, G. Hernandez-Sosa
Institute of Microstructure Technology
Karlsruhe Institute of Technology
Hermann-von-Helmholtz-Platz 1, 76344 Eggenstein-Leopoldshafen, Germany

The ORCID identification number(s) for the author(s) of this article can be found under https://doi.org/10.1002/adom.202102397.

DOI: 10.1002/adom.202102397

OPDs in comparison to silicon-based devices. Furthermore, in the case of donor–acceptor systems, the relative orientation of two (macro-)molecular species at the interface can be used to modify charge-transfer state formation, charge separation and photocurrent generation.[21–24]

Orientation of thin, ≈100 nm semiconducting polymer films is commonly achieved by postdeposition high-temperature mechanical rubbing, yielding dichroic ratios (DRs) up to 9 for benchmark materials.[25–27] However, this inherently macroscopic approach is unsuitable for the fabrication of miniaturized devices, or complex arrays thereof, while the propensity for mechanical damage of delicate molecular active layers leads to severe device shunting and prohibitively high dark currents.[27] Alternative approaches utilizing alignment layers[28] are less well studied and are likely to introduce severe constraints to the possible device architectures.

Hence, in the present work we employ the so-called "crystallizable" solvents[25,29–32] for enabling on-demand directional orientation of organic semiconductors. With foresight to subsequent extension to inkjet-printing fabrication,[31] we devise an entirely solution-based fabrication approach based on air-assisted blade-coating for the deposition of oriented donor–acceptor blends. Furthermore, we advance a novel processing strategy for dark current suppression[33] within fibrillar active layers via backfilling with an insulating polymer followed by plasma etching to ameliorate the drawbacks of surface roughness. The characteristics of polarized all-polymer OPDs based on classical polymeric donor–acceptor materials are explored in detail and the generality of the processing method is demonstrated by extending the approach to oriented polymer donor blends with small-molecular nonfullerene acceptors (NFAs). Finally, as a proof-of-concept application we present polarimetry-inspired analysis of the photoelastic response of natural rubber films to tensile deformation, highlighting the potential of polarized OPDs for advanced optical sensing.

2. Results and Discussion

2.1. Materials and the State of the Art

As our model system, we employ the materials shown in **Figure 1**a. Poly(3-hexylthiophene) (P3HT) is chosen as the benchmark polymer donor, while N2200 (alternatively referred to as "P(NDI2OD-T2)")[20,27,34–36] is selected as the polymer acceptor owing to its complementary optical absorption and compatible highest occupied molecular orbital (HOMO) and lowest unoccupied molecular orbital (LUMO) energy levels (Figure 1b). 1,3,5-Trichlorobenzene (TCB) is chosen as the prototypical crystallizable solvent which exhibits the requisite needle-like crystal growth, low melting temperature of 63 °C and rapid sublimation at ambient conditions that facilitates its post-deposition removal. Epitaxial solidification of P3HT onto TCB crystals has been reported previously[25,29–31] and was rationalized by the close epitaxial match between the *d*-spacing of P3HT along the backbone and the fast growth axis of TCB crystals ($c_{P3HT}/2 \approx 3.8$ Å; $c_{TCB} \approx 3.9$ Å).[29] Gratifyingly, the *d*-spacing along the N2200 backbone is close to an integer multiple of that of P3HT ($c_{N2200} \approx 14.4$ Å $\approx 2 \times c_{P3HT}$)[36] which implies that directional epitaxial crystallization of both polymers can be realized by

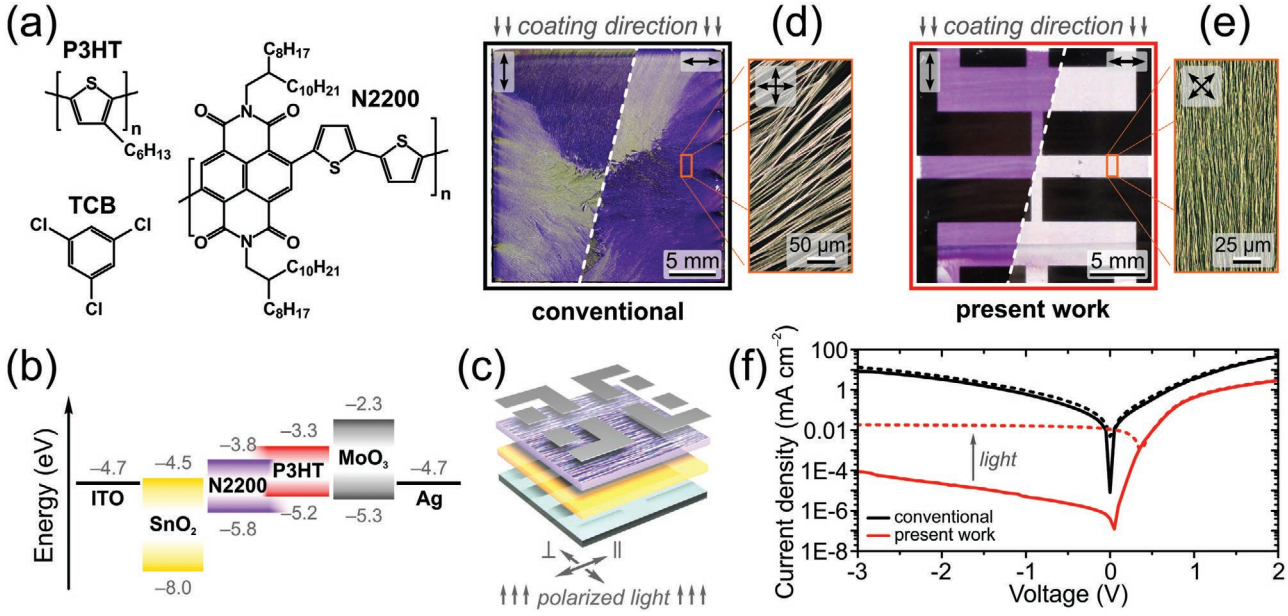

Figure 1. a) Chemical structures of the studied materials. b) Energy level diagram of an OPD employing a P3HT:N2200 polymer blend bulk heterojunction as the active layer and c) the corresponding device architecture. Also shown are the photographs of P3HT:N2200 films blade-coated from d) "conventional"[30] solutions containing the crystallizable solvent TCB and e) the method developed in the present work. Images were recorded under illumination polarized parallel and perpendicular to the coating direction (as indicated by ↔) and highlight different degree and directionality of chain orientation. The respective cross-polarized images shown in the insets reveal the presence of interfibrillar "pinholes" for the conventionally deposited film (black areas in the image) and a comparatively dense fibrillar microstructure obtained by the present method. f) *J*–*V* curves for photodiodes based on the films shown in (d,e) measured in the dark (solid lines) and under unpolarized illumination at 520 nm (15 mW cm^{-2}; dotted lines).

co-deposition with TCB. Hence, following initial screening of different OPD geometries, we select the inverted device architecture depicted schematically in Figure 1c, comprising indium tin oxide (ITO) cathode, SnO_2 hole-blocking interlayer, P3HT:N2200 bulk heterojunction, MoO_3 hole-extraction interlayer and silver anode.

Figure 1d shows images recorded under polarized illumination for a P3HT:N2200 blend film fabricated "conventionally,"[30] that is, by blade-coating semiconductor blend solutions in a chlorobenzene:TCB mixture. Clearly, the resulting film features two noteworthy drawbacks. First, the variation of colors with respect to the coating direction indicates that chain orientation is not directional, with nucleation primarily initiated at the rough substrate edges. Second, as shown by the inset cross-polarized image in Figure 1d, the film is not "closed" (i.e., spatially discontinuous), exhibiting a coarse fibrillar microstructure with prominent interfibrillar "pinholes" appearing as dark regions. The latter contribute shunt paths in the OPD active layers, leading to poor diode characteristics and virtually indistinguishable reverse-bias response in the dark and under illumination (Figure 1f, black curves).

Hereafter we aim to address these limitations and advance a method for i) obtaining controllable directional orientation of organic semiconductor active layers (see exemplary polarized-illumination images in Figure 1e) and ii) suppressing dark current in the resulting devices, as illustrated by the corresponding *J–V* data in Figure 1f (red curves).

2.2. Directionally Oriented Films

Orientation by directional epitaxial crystallization has two requisites: the first is the above-mentioned epitaxial match, and the second is that TCB crystallizes prior to the organic semiconductors. For the orientation of growing TCB crystals to maximally coincide with the blade-coating direction, their nucleation must be initiated in the immediate vicinity of the blade as it moves across the substrate. Furthermore, manipulating the rate of TCB solidification to enable faster crystallization kinetics will reduce the size of individual TCB fibrils (as, indeed, observed for the closely related polyolefin/clarifying-agent material systems[37]) and avoid the formation of an excessively coarse thin-film microstructure.

The first step, therefore, is to prepare solutions in chloroform (CF) instead of the more commonly employed chlorobenzene (T_b = 61 and 132 °C, respectively). However, this in itself was found to be generally insufficient for enabling directional orientation of the semiconducting polymers. Hence, in our method we use an electric fan placed adjacent to the blade to further accelerate solvent evaporation during deposition (see photographs of setup in Figure S1, Supporting Information).

This simple extension to *air-assisted blade-coating* proves to be effective for yielding highly oriented films. A comprehensive examination of the influence of various process parameters[38,39] (e.g., chloroform:TCB ratio, coating speed, chemical structure and blending ratio of different polymers) on the optical anisotropy, microstructure and topography of the resulting films is presented in Figures S2–S8 in the Supporting Information. Briefly, film formation is found to occur in so-called "evaporative regime" instead of the classical Landau–Levich regime[30,39] owing to rapid supersaturation of solutions and, hence, a TCB/polymer crystallization front that closely follows the moving blade. Optical anisotropy is primarily governed by chloroform:TCB ratio (optimally 1 : 0.2–0.4 w/w) and coating speed (optimally 5–8 mm s^{-1}). Interestingly, our findings indicate that the orientation process is more complex than previously believed.[25] For instance, despite equivalent *d*-spacing along the backbone, dodecyl- ($C_{12}H_{25}$) substituted poly(3-alkylthiophene) is found to orient *perpendicular* to the coating direction, unlike the butyl- (C_4H_9) and hexyl- (C_6H_{13}) substituted derivatives (Figure S6, Supporting Information). Such rarely observed[40] dependence of preferential orientation axis on side-chain length highlights the versatility of employing crystallizable solvents for obtaining a diverse range of chain-oriented microstructures.

Figure 2a shows polarized images for a 120-nm-thick oriented P3HT:N2200 film (as in Figure 1e). The contrast between images recorded with incident light polarized parallel and perpendicular to the coating direction indicates both the uniformity of chain orientation with respect to the coating direction and the high resulting optical dichroism. The cross-polarized image highlights the "closed," dense fibrillar microstructure as opposed to the isolated fiber bundles obtained for a "conventionally" deposited film (cf. inset of Figure 1d).

Polarized absorption spectra shown in Figure 2b confirm preferential orientation of conjugated polymer backbones along the coating direction. The corresponding DR spectrum, calculated as the ratio between parallel- and perpendicular-polarized absorption, shows the expected increase of DR at the low-energy side of the respective P3HT (450–650 nm) and N2200 (650–850 nm) absorption features, indicating that maximal uniaxial alignment is obtained for crystalline chain segments.[16,30] P3HT exhibits the highest maximum DR, while a marginally lower value is observed for N2200 (DR_{max} = 5.9 and 3.1, respectively). The latter can be ascribed to partial preaggregation of N2200 in solutions[35] and higher epitaxial miss ratio with TCB (c_{P3HT} : $2c_{TCB}$ = 0.01; c_{N2200} : $4c_{TCB}$ = 0.05). Given that higher DR values for N2200 are obtained upon reducing its concentration in solutions (Figure S7, Supporting Information), the former scenario is considered more likely.

Grazing-incidence wide-angle X-ray scattering (GIWAXS) is used to gain further structural information on the oriented P3HT:N2200 films, including the π-stacking and interlayer distances, long-range crystalline order and polymer backbone orientation relative to the substrate. Figure 2c shows the GIWAXS pattern recorded for a 300-nm-thick oriented film with the beam aligned perpendicular to the coating direction (i.e., perpendicular to the polymer orientation axis). The intense reflections seen in Figure 2c confirm the crystalline microstructure of the oriented films. Given that both polymers are extensively described in the literature, [20,25,31,36] we directly focus on their crystalline arrangement within oriented blend films. In the *out-of-plane* direction (q_{xy} = 0 $Å^{-1}$; Figure 2d), the intense first-order reflection associated with an interlayer distance of 1.71 nm is located at q_z = 0.36 $Å^{-1}$. This out-of-plane peak position is characteristic of *edge-on* orientation of P3HT.[41] Higher order (200) and (300) reflections suggest the existence of long-range order

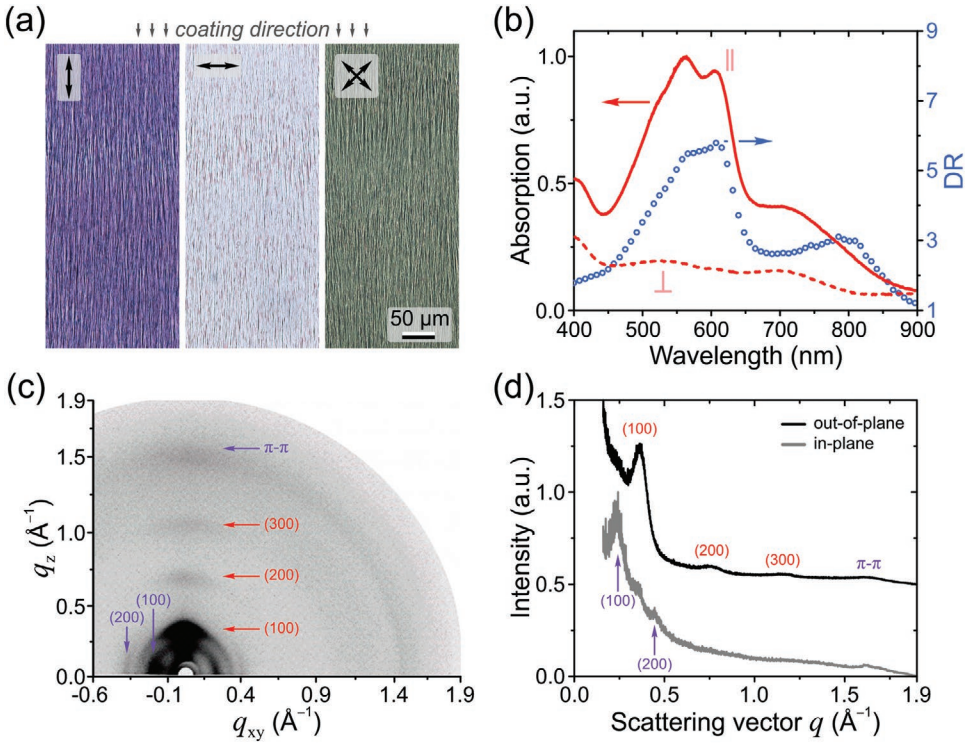

Figure 2. Optical anisotropy and microstructure of oriented P3HT:N2200 films. a) Transmitted-light polarized and cross-polarized images (as indicated by ↔) for a 120-nm-thick film. b) Polarized absorption spectra for the same film recorded with the incident light polarized parallel and perpendicular to the coating direction (solid and dotted red lines; left ordinate). Also shown is the corresponding dichroic ratio spectrum (red circles; right ordinate). c) 2D-GIWAXS pattern for a 300-nm-thick oriented film and d) the corresponding in-plane (q_{xy}) and out-of-plane (q_z) profiles. P3HT (red) and N2200 (purple) reflections are indicated.

for the P3HT lamellar structure. One additional reflection located in out-of-plane direction with *d*-spacing ≈0.39 nm was observed at q_z = 1.61 Å^{-1} and is assigned to the π-stacking distance of N2200. The location of the π-stacking reflection in the out-of-plane direction is indicative of *face-on* orientation of N2200. This type of organization is additionally confirmed by the reflection observed in the *in-plane* direction (q_z = 0 Å^{-1}; Figure 2d) at q_{xy} = 0.24 Å^{-1} which is assigned to the characteristic interlayer distance of 2.55 nm for N2200.[42] The higher order (200) reflection confirms long-range organization of N2200.

The long-range order was further analyzed through the calculation of (100) coherence lengths (d_{CL}) on the basis of the Scherrer equation from peak fits to the out-of-plane (P3HT) and in-plane (for N2200) GIWAXS data shown in Figure 2c. Both polymers feature relatively high coherence lengths (d_{CL} = 32 and 15 nm for P3HT and N2200, respectively), indicating their substantial phase separation in the oriented films. The observed packing motifs (edge-on for P3HT and face-on for N2200) and *d*-spacings are in agreement with the literature, which includes the possibility of partial vertical phase separation.[20] Summarizing the GIWAXS part, we conclude that the oriented films exhibit a favorable bulk heterojunction microstructure with nanoscale donor–acceptor phase separation as well as macroscopically unidirectional polymer organization with predominantly edge-on and face-on orientation of crystalline P3HT and N2200, respectively.

2.3. Backfilling and Dark-Current Suppression

While the dense fibrillar microstructure obtained by air-assisted blade-coating (cf. Figure 1d,e) reduces the presence of shunt paths and improves *J*–*V* characteristics compared to "conventionally" deposited oriented active layers (Figure S9, Supporting Information), we seek further dark-current suppression via a post-processing method based on backfilling and subsequent etching. Specifically, we select *plasma etching*, since it offers numerous advantages over the alternative "wet" chemical etching approaches in terms of high process precision and elimination of chemical waste.[43]

The idealized illustration of the process is shown in **Figure 3**a. The as-deposited oriented films exhibit substantial surface roughness following sublimation of TCB, with typical root mean square values up to 30 nm. A film of an electrically insulating polymer is then spin-coated on top from solutions in orthogonal solvents to provide "backfilling" of the potential shunt paths. Finally, plasma treatment is used to etch away a given thickness of the backfilling layer to optimally recover the semiconductor interface for subsequent electrode deposition. Key, therefore, is the selection of materials and process parameters that will yield suitably balanced etching rates without degradation of the semiconductors' optoelectronic characteristics.

Polystyrene (PS) and poly(methyl methacrylate) (PMMA) were investigated as potential backfilling materials given their solubility in orthogonal solvents and equivalent dielectric

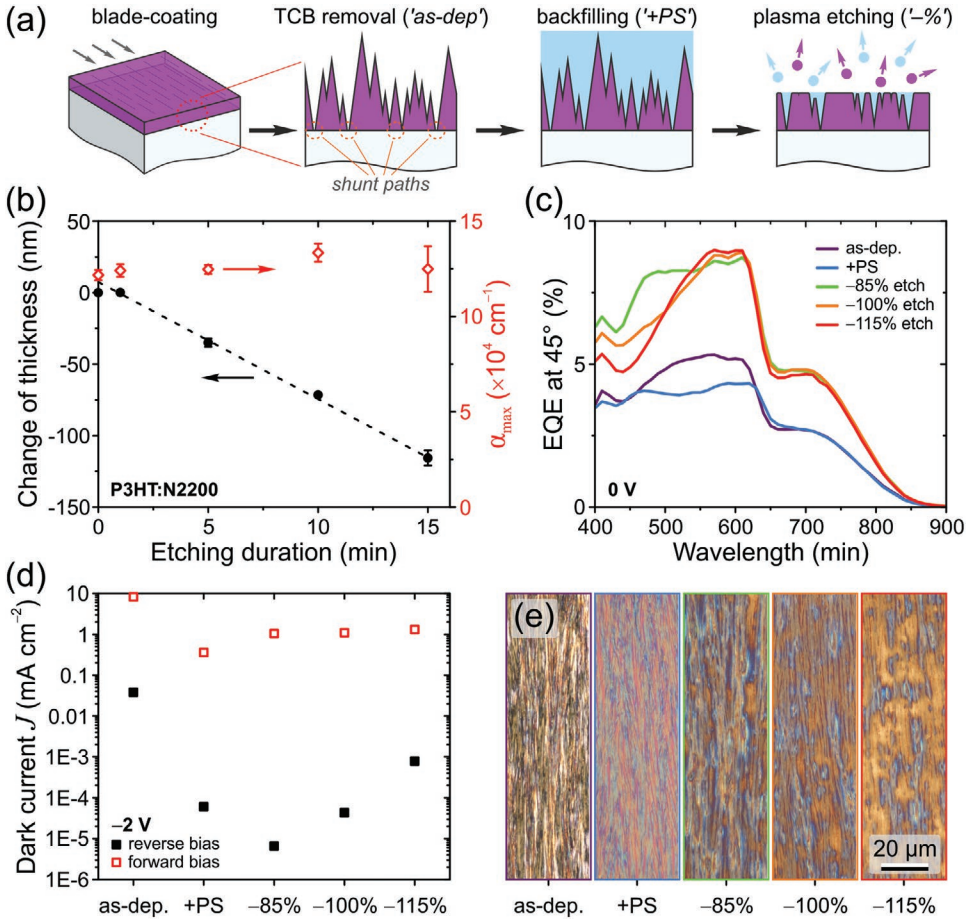

Figure 3. Dark-current suppression. a) Schematic illustration of the backfilling and plasma etching process. b) Change of thickness for a P3HT:N2200 film as a function of O_2 plasma etching duration (solid black circles; left ordinate) and the corresponding values of maximum absorption coefficient, α_{max} (open red diamonds; right ordinate). Also shown are the data for 120-nm-thick polarized P3HT:N2200 OPDs: c) EQE spectra recorded with incident light polarized at 45° relative to the orientation axis, d) dark-current density J measured at reverse and forward bias of 2 V, and e) the corresponding reflected-light images. In all cases, data are shown for devices based on as as-deposited ("as-dep.") active layers, the same active layers after backfilling with polystyrene ("+PS"), and following plasma etching of –85%, –100%, and –115% of the initially deposited PS thickness.

breakdown strength (3–5 kV mm^{-1} for film thickness <10 µm).[44] Etching rates were determined from linear fits to the change of film thickness as a function of plasma etching duration for reference spin-coated films (see example for P3HT:N2200 in Figure 3b). The values summarized in **Table 1** exhibit trends that are consistent with previous reports, namely: higher etching rates for all materials in the reactive O_2 plasma[45] and lower etching rates for materials with a high density of aromatic groups (P3HT:N2200 and PS).[46] Hence, PS is selected as the optimal backfilling material due to exhibiting a balanced etching rate with the P3HT:N2200 blend and O_2 plasma is chosen for enabling maximal etching rates.

Table 1. Linear O_2 and Ar plasma etching rates for the polymers used in this study.

Plasma	Etching rate [nm min^{-1}]		
	P3HT:N2200	PS	PMMA
Oxygen	7.5 ± 0.4	7.1 ± 0.1	22.5 ± 0.2
Argon	3.9 ± 0.3	1.3 ± 0.2	5.9 ± 0.3

Most importantly, no appreciable degradation of the semiconductors is observed following plasma treatment. Illustrating this, the maximum value of absorption coefficient measured for P3HT:N2200 films at 558 nm is found to be invariant with O_2 plasma etching duration (Figure 3b). As a further confirmation, external quantum efficiency (EQE) spectra in Figure 3c show that *polarization-average* EQE recorded with light polarized at 45° relative to the orientation axis is, in fact, enhanced following PS backfilling and plasma etching. Finally, we note that care must be taken when selecting etching conditions since prolonged O_2 plasma etching can itself yield an increase in film roughness, as illustrated in Figure S10 in the Supporting Information.

Having established the backfilling process, we now examine its impact on the dark-current characteristics of OPDs based on oriented P3HT:N2200 films. Figure 3d shows that the reverse dark-current density, J_D, of as-deposited ("as-dep.") devices at –2 V is reduced by nearly three decades after backfilling with PS ("+PS"). Despite the presence of the insulating PS layer, the device still functions as a diode, which is ascribed to conducting pathways originating from the high roughness of the

active layer and local dielectric breakdown occurring at the thinnest PS regions. As expected, plasma etching leads to a gradual increase in J_D that is proportional to the percentage of the initial PS thickness removed by etching. Nevertheless, the device processed with PS backfilling and subsequent etching of –100% of the initial PS layer thickness features a J_D of 4.3×10^{-5} mA cm^{-2} at –2 V, which is strongly suppressed in comparison to the respective value of 3.8×10^{-2} mA cm^{-2} for the as-deposited device. In the forward regime of the *J–V* curves, PS backfilling leads to a minor reduction of current density due to PS acting as an electron-injection barrier. For completeness, the full *J–V* curves are shown in Figure S9 in the Supporting Information.

To confirm that J_D suppression in backfilled and etched OPDs originates from the presence of residual PS, the corresponding optical microscopy images are shown in Figure 3e. Comparison of the images across the series highlights the presence of blue-colored regions in, most evidently, backfilled samples with –100% and –115% etching. These regions are oriented vertically along the coating direction and are selectively removed by immersion in ethyl acetate (Figure S11, Supporting Information), confirming that they correspond to PS. For completeness, atomic force microscopy (AFM) images showing the topography of oriented films following backfilling and plasma etching are presented in Figure S11 in the Supporting Information. Finally, we note that PS backfilling implies that the J_D values reported in Figure 3d represent the upper limit because the actual device area is reduced by the presence of PS regions at the semiconductor:anode interface.

2.4. Polarized Photodetectors

2.4.1. P3HT:N2200 OPDs

The characteristics of a polarized OPD based on a 120-nm-thick oriented P3HT:N2200 active layer post-processed with PS backfilling and –100% etching for J_D suppression are presented in **Figure 4**a–d. Comparisons are made throughout with the respective data for a nonoriented (hereafter termed "isotropic") OPD based on a spin-coated blend film of similar thickness.

Spectral responsivity, $R(\lambda)$, data are shown in Figure 4a. Anisotropic responsivity is observed for the polarized OPD, with the *polarization ratio* (PR; ratio of $R(\lambda)$ recorded with parallel- and perpendicular-polarized light) reaching 3.2 for the P3HT band at 580 nm. Comparison of polarized responsivity and absorption spectra (cf. Figure 4a and Figure 2b) reveals a number of important differences. First, the maximum PR value of 3.2 is substantially lower than the corresponding DR value of 5.9. Second, while anisotropic *absorption* is observed for both P3HT and N2200 bands, the *spectral responsivity* for the N2200 band is essentially unpolarized (PR < 1.5; see detailed comparison in Figure S12, Supporting Information). Overall, the maximum PR values are a factor of 2 lower than the respective DR values. This indicates that exciton dissociation is accompanied by depolarization processes which, although unclear at present, may be related to a restricted charge generation and transport for a donor–acceptor interface featuring edge-on and face-on orientations of the respective materials.[47] Moreover, this process is found to depend on the specific donor–acceptor system, as will be shown below.

The isotropic OPD exhibits a markedly lower spectral responsivity—comparable to that of polarized OPD under perpendicular-polarized illumination. The difference is attributed to the enhancement of charge-carrier mobility for macroscopically ordered semiconductor materials,[17–20] which thus allows for more efficient charge extraction prior to recombination for polarized OPDs. Finally, we note that the active layer thickness itself influences both photocurrent (increases marginally for thicknesses ≥170 nm) and polarization ratio (decreases for thicknesses >120 nm), as shown in Figure S12 in the Supporting Information. The decrease of optical anisotropy and polarization ratios for active layer thickness >120 nm is ascribed to the progressively slower drying of thicker donor–acceptor blend films, resulting in less uniformly directional chain orientation, as illustrated by the images in Figure S12e in the Supporting Information. The optimal trade-off for polarized P3HT:N2200 OPDs is obtained for 120 nm thick active layers, as in Figure 4a.

Figure 4b shows that the postprocessing scheme employed for J_D suppression in polarized OPDs yields reverse-bias dark-current densities that are comparable to, and even lower than, those of isotropic devices. This has significant practical relevance since OPDs are typically operated under reverse bias to facilitate charge extraction, whereby higher spectral responsivities can be obtained (see example in Figure S12c, Supporting Information).[5] To benchmark the performance of polarized P3HT:N2200 OPDs, the frequency-independent specific detectivity D^* (that is, D^* in the central frequency range dominated by white noise[5]) was estimated as

$$D^*(\lambda) \approx \frac{R(\lambda)\sqrt{A}}{\sqrt{2ei_{\text{dark}} + 4k_B T R_{\text{shunt}}^{-1}}} \approx \frac{R(\lambda)}{\sqrt{2e}\sqrt{J_D}} \quad (1)$$

where $R(\lambda)$ is the spectral responsivity, A is the device active area, e is elementary charge, i_{dark} is the dark current under a given reverse bias, T is temperature, and R_{shunt} is the shunt resistance of the OPD (assumed to be infinite in the second part of Equation (1)). Given these approximations, the results shown in Figure 4c thus represent the maximum achievable specific detectivities. The maximum D^* of 7×10^{11} Jones (cm Hz$^{1/2}$ W^{-1}) obtained for the polarized OPD under parallel-polarized illumination and 2 V reverse bias represents a threefold improvement over the respective value for the isotropic OPD. Nevertheless, the overall D^* values remain moderate in comparison to state-of-the-art isotropic OPDs[4] which is ascribed to the limited efficiency of the selected all-polymer bulk heterojunction blend.[34,35]

The linear dynamic range, representing the span of the linear regime of photocurrent response to illumination intensity, for 120-nm-thick polarized OPDs is estimated to be ≥85 dB which approaches the state-of-the-art values reported for high-performance OPDs.[5] The corresponding analysis, including representative *J–V* curves under varying illumination intensities, is shown in Figure S13 in the Supporting Information.

Yet another key figure of merit for OPDs is their detection speed which is typically quantified by a metric termed the "3 dB cutoff frequency," $f_{3\text{dB}}$, i.e., the modulation frequency

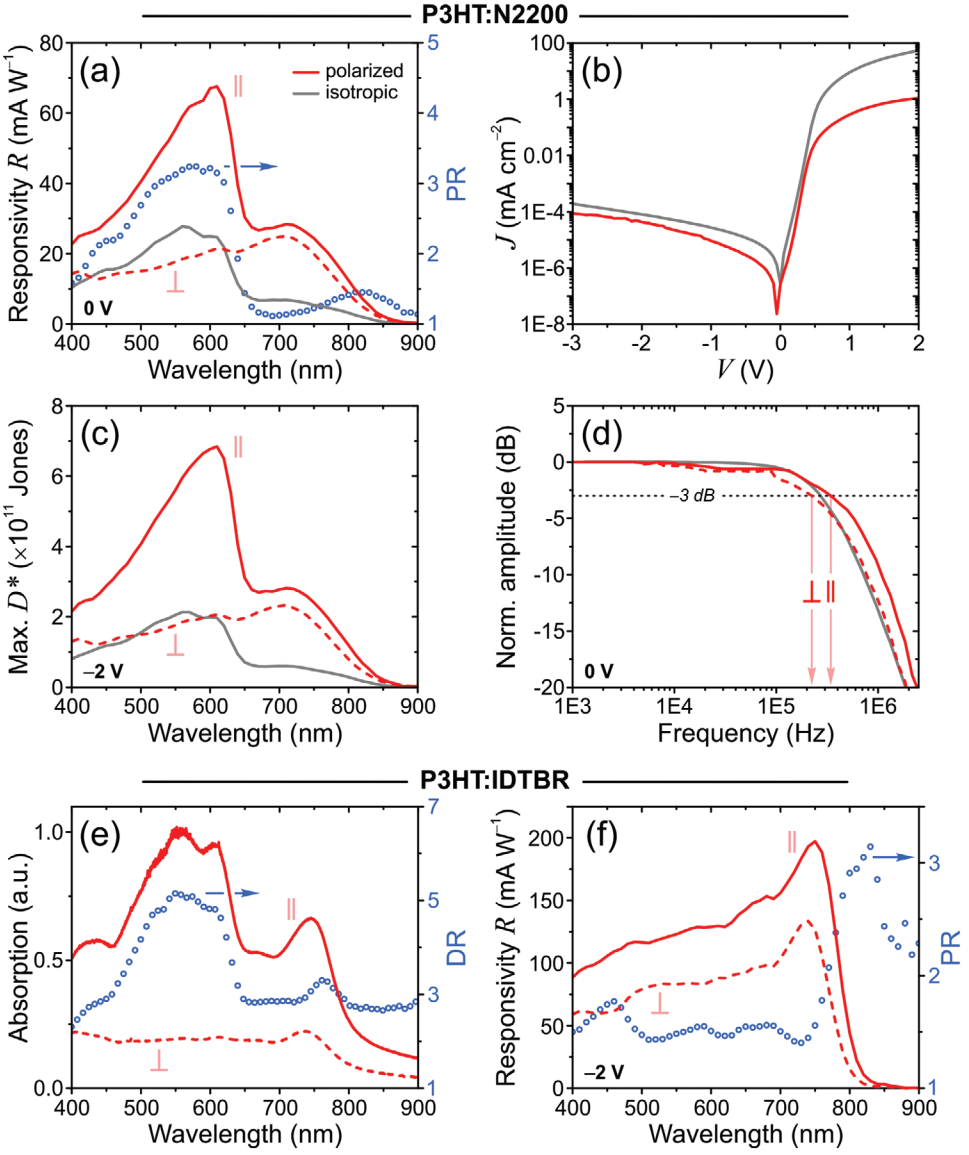

Figure 4. OPD characteristics for polarized (red lines) and isotropic (gray lines) devices. Top and middle panels: P3HT:N2200 OPDs (thickness ≈120–140 nm; polarized OPDs employed PS backfilling and –100% etching for J_D suppression). a) Spectral responsivity $R(\lambda)$ and the corresponding polarization ratio PR (blue circles; right ordinate). b) Dark J–V characteristics. c) Maximum specific detectivity D^* at –2 V. d) Cutoff frequency measurements, with the 3 dB cutoff frequency indicated. Bottom panels: The corresponding data for polarized P3HT:IDTBR OPDs (thickness ≈210 nm; PMMA backfilling employed) showing e) polarized absorption spectra and f) spectral responsivity at –2 V as well as the respective DR and PR values. In all cases, data recorded with incident light polarized parallel and perpendicular to the orientation axis are shown by solid and dotted lines respectively.

of the illumination signal for which the photocurrent reduces to 70% of its steady-state value.[5] One of the principal factors restricting high-frequency operation of OPDs is the limited charge-carrier mobility within the active layer materials which, in turn, is governed by their solid-state microstructure.[17–20] Figure 4d and **Table 2** show that the polarized OPD exhibits a substantially higher cutoff frequency for parallel-polarized excitation compared to the isotropic OPD. The impact of chain orientation and the resulting enhancement of long-range photocarrier transport is also evident from comparison of f_{3dB} values obtained for the polarized OPD under parallel and perpendicular polarizations which show an anisotropy of 1.5. In fact, a nearly threefold increase in f_{3dB} relative to the isotropic OPD is found for the polarized OPD, for which PS backfilling was employed *without* subsequent etching (Table 1 and Figure S14, Supporting Information). The resulting 3 dB cutoff frequency of 0.75 MHz recorded under parallel-polarized light is among the highest reported for all-polymer OPDs to-date.[48]

Overall, the demonstrated fabrication method for directional chain orientation and backfilling yields OPDs that not only exhibit polarized detection but also an enhancement of principal figures of merit such as spectral responsivity, specific detectivity, and detection speed.

Table 2. 3 dB cutoff frequency values for polarized and isotropic P3HT:N2200 OPDs measured under parallel- and perpendicular-polarized excitation at 0 V bias.

Sample	3 dB cutoff frequency [MHz]	
	parallel	perpendicular
Polarized; +PS –100%	0.34	0.22
Polarized; +PS	0.75	0.26
Isotropic	0.28	0.26

2.4.2. P3HT:IDTBR OPDs

To demonstrate the generality of the fabrication method reported herein beyond the specific example of P3HT:N2200 blends, the processing scheme was applied to P3HT blends with the small-molecular NFA IDTBR (i.e. 5,5'-[[4,4,9,9-Tetraoctyl-4,9-dihydro-s-indaceno[1,2-b:5,6-b']dithiophene-2,7-diyl]bis(2,1,3-benzothiadiazole-7,4-diylmethylidyne)] bis[3-ethyl-2-thioxo-4-thiazolidinone]). Two minor processing adjustments were made. First, the backfilling material was changed to PMMA given the absence of orthogonal solvents for PS and IDTBR. Second, given the difference between O_2 plasma etching rates for PMMA and the semiconductors (Table 1), no plasma treatment was performed following deposition of 60 nm PMMA backfilling layers onto oriented P3HT:IDTBR films. Although this simplified processing results in substantially poorer *J–V* characteristics (Figure S15, Supporting Information) than for backfilled and etched P3HT:N2200 devices, the overall OPD performance can be evaluated nevertheless.

Polarized absorption spectra for 210 nm thick P3HT:IDTBR OPDs shown in Figure 4e reveal a broadband absorption anisotropy, with DR > 2.7 across both donor and acceptor absorption bands, peaking at 5.2 for P3HT. This is especially remarkable given the absence of a clear epitaxial match between TCB and the unit cell parameters of IDTBR (a = 13.77 Å, b = 15.81 Å, c = 32.71 Å),[49] indicating that lattice matching does not play the determining role in enabling directional (macro-)molecular orientation. The corresponding polarized spectral responsivity data in Figure 4f similarly shows a broadband anisotropy, albeit limited to polarization ratios ≈1.5 across most of the wavelength range for these unoptimized devices. The key noteworthy feature is that the highest PR in excess of 2.5 is obtained at the low-energy side of the acceptor band of P3HT:IDTBR OPDs, in contrast to the N2200 band which is essentially unpolarized in P3HT:N2200 OPDs (Figure 4a and Figure S12d, Supporting Information). This difference suggests that polarized OPDs fabricated by the present method can exhibit a variety of application-specific polarization sensitivities that may be selected to be broad- or narrow-band by the specific material system.

2.5. Applications in Photoelasticity Analysis

To demonstrate the application potential of polarized OPDs reported in this work, we perform exemplary photoelasticity analysis[50,51] of natural rubber under uniaxial extension. The commercial-grade material used herein is transparent in the visible spectral range but features a substantial transmission haze (Figure S16, Supporting Information) due to the presence of crystallites, surface roughness, and the possible use of fillers.[52] As such, natural rubber is representative of a broad class of elastomeric materials used in numerous applications, including emerging technologies requiring soft platforms for wearable electronic devices in haptics, human–machine interfacing, and medicine.[53]

Figure 5a shows images of a natural rubber film at increasing draw ratios Λ (ratio of final and initial sample lengths) recorded in cross-polarized geometry—that is, with incident and transmitted light polarized at ±45° with respect to the drawing axis. While the unstretched (Λ = 1) film is largely isotropic and dark between crossed polarizers, transmission of light is subsequently enabled due to birefringence arising from non-isotropic distribution of macromolecules upon uniaxial extension. (Cross-polarized imaging of the sample during extension and relaxation cycles is shown in Movie S1, Supporting Information.) The observed colors of transmitted light are not arbitrary but rather correspond to specific birefringence, as can be quantified from the Michel-Lévy chart,[51] and, therewith, mechanical stress in the sample. Illustrating this, Figure 5b shows the stress–strain data for the same data which exhibits the typical nonlinear S-shape of rubber materials above the glass transition temperature. Tensile stress increases sharply for Λ > 6 due to strain-induced crystallization,[54] signifying that the sample approaches its maximum strain. The transition between two regimes is fully consistent with the cross-polarized images in Figure 5a which reveal the appearance of colored fringe patterns for Λ > 6 that are indicative of stress distribution.

Polarized P3HT:N2200 OPDs (120 nm thick; PS backfilling used) were tested in the crosspolarized geometry shown in Figure 5c. The orientation axis of the polarized OPD was positioned at 90° relative to the incident polarized white light, with the natural rubber film prestretched to a given draw ratio placed in the middle. Spectral responsivity was then recorded at three wavelengths with the drawing axis of the rubber sample positioned at 45° and 90°. In the 45°-oriented position the rubber sample directs the transmitted interference light parallel to the orientation axis of the OPD, leading to an increase in the detected photocurrent. Birefringence effects are not observed for the 90°-oriented position of the rubber sample which therefore provides a reference for draw-ratio-dependent variations of sample thickness and haze (Figure S16, Supporting Information).

Figure 5d shows the ratio of spectral responsivities, ΔR, measured with the rubber sample oriented at 45° and 90° as a function of draw ratio. Comparison of ΔR values, transmitted light colors in Figure 5a and OPD polarization ratios for the three wavelengths (as indicated in Figure 5d) reveals a number of salient features. First, ΔR increases for all wavelengths up to Λ ≈ 4–6 due to increasing birefringence. The highest ΔR increase is observed at 630 nm which corresponds to the spectral position of the highest polarization ratio for the OPD (Figure S16, Supporting Information). Second, ΔR exhibits a roll-off for Λ ≥ 6 which is ascribed to reduced overall intensity of the transmitted light upon transition into strain-induced crystallization regime. Third, the absolute decrease of ΔR for Λ ≥ 6 appears to be related to the specific interference colors,

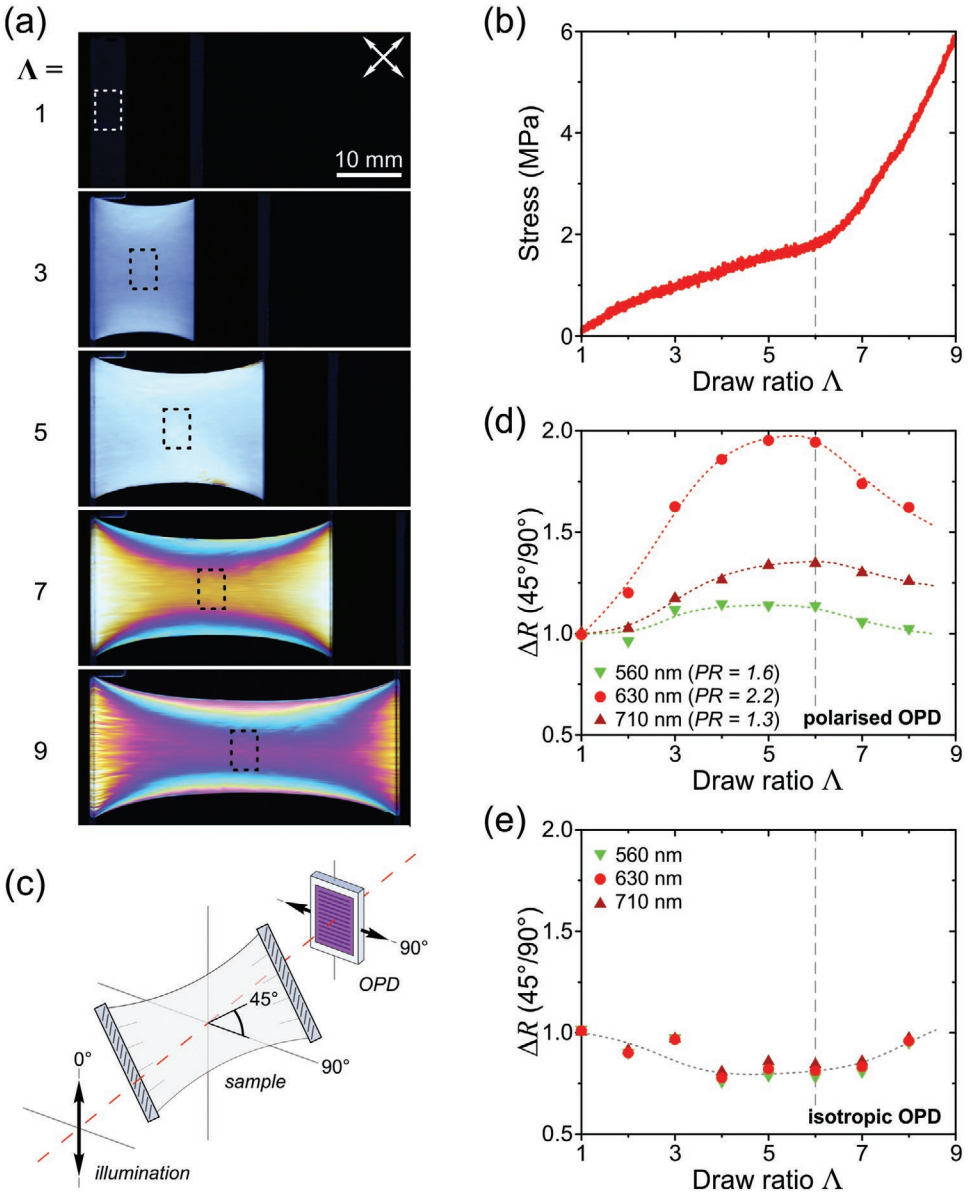

Figure 5. a) Cross-polarized images of a natural rubber film at different draw ratios, Λ, and b) tensile-test data for the same film, showing stress as a function of Λ. c) Imaging configuration used for photoelasticity analysis using P3HT:N2200 OPDs. d,e) Ratio of spectral responsivities, ΔR, recorded with the stretched rubber film rotated at 45° and 90° with respect to incident light polarization. Data are shown for d) polarized and e) reference isotropic OPDs under white-light illumination. Representative ΔR values are shown for 560, 630, and 710 nm (the respective polarization ratios, PR, are indicated in (d)), normalized by the respective values at $\Lambda = 1$.

as well as their sequence. For instance, the progression of first-order interference colors in the Michel-Lévy chart is white, yellow, orange, and magenta/red.[51] Hence, ΔR at 560 nm peaks at the lowest draw ratio ($\Lambda \approx 4$) and exhibits maximum roll-off, reaching ≈1 at $\Lambda = 8$, due to the redshift of transmitted light. On the contrary, the minimum roll-off is found for ΔR at 710 nm, which also features a peak at the highest draw ratio ($\Lambda \approx 6$). Reassuringly, the same analysis performed with an isotropic P3HT:N2200 OPD (Figure 5e) shows only a minor variation of ΔR with Λ and no wavelength dependence.

While a further in-depth exploration of photoelasticity analysis is beyond the scope of the present work, the results clearly demonstrate the broad potential for application of polarized OPDs. For instance, polarized OPD arrays can be used for polarimetry and photoelasticity imaging in process- and quality-control monitoring, wherein quantitative mapping of color fringe patterns can highlight local changes in stress distribution arising from internal defects[50,55] (see examples for a natural rubber film in Figure S17 and Movie S2, Supporting Information). Besides these existing industrial applications, the adaptation of miniaturized arrays of polarized OPDs to flexible substrates can also provide advanced optical sensing for emerging technologies in the field of wearable, flexible, and stretchable electronics.

3. Conclusion

In summary, we have demonstrated polarization-sensitive OPDs based on directionally oriented active layers. The resulting polarized P3HT:N2200 OPDs exhibited an overall enhancement of spectral responsivity and specific detectivity compared with reference isotropic devices, as well as up to a threefold increase in detection speed and maximum polarization ratios of ≈3.5. The choice of donor–acceptor materials was also shown to govern both the absolute polarization sensitivity and its spectral coverage, with broadband polarization response found for polymer:NFA (i.e., P3HT:IDTBR) OPDs and predominantly donor-only polarization for P3HT:N2200. The oriented films were obtained by a versatile air-assisted blade-coating method that is adaptable to both polymer:polymer and polymer:NFA donor–acceptor blends. To compensate for the high roughness of fibrillar oriented active layers, a postprocessing scheme based on backfilling and subsequent plasma etching was presented, enabling reverse dark-current suppression by over three orders of magnitude. Finally, we have confirmed the application potential of these devices by polarimetry-inspired analysis of the photoelastic response of natural rubber films under tensile stress. Looking ahead, the low-cost fabrication, tunable polarization sensitivity, and suitability for low-light operation make polarized OPDs highly suited for advanced optical sensing in existing and emerging applications.

Future work will aim to explore the depolarization phenomena underpinning the nontrivial correlation between optical and photocurrent anisotropy observed for polarized OPDs as well as test the performance of oriented donor–acceptor bulk heterojunctions in photovoltaic devices. The enabling role of epitaxy on directional orientation will be investigated for model material systems. The extension of materials processing to high-throughput methods such as inkjet printing will also be targeted for constructing complex polarized OPD arrays.

4. Experimental Section

Materials: P3HT (M_w ≈ 58 000 g mol^{-1}, polydispersity index (PDI) = 2.1, regioregularity (RR) > 96%) was purchased from Rieke Metals. N2200 (Chemical Abstracts Service (CAS) No.: 1100243-40-0; M_w ≈ 150 000 g mol^{-1}, PDI = 2–3, RR > 99%) and o-IDTBR (CAS No.: 2077945-91-4) were purchased from 1-Material. PS (M_w ≈ 35 000 g mol^{-1}) and TCB were purchased from Sigma-Aldrich. PMMA (M_w ≈ 15 000 g mol^{-1}) was purchased from Acros Organics. SnO_2 dispersion ("N-31") was purchased from Avantama. Standard laboratory-grade solvents were used. Natural rubber specimens were cut from a commercial latex condom (Durex) and cleaned with isopropanol to remove surface additives. All other materials were used as received. The details of additional materials are given in the Supporting Information.

Thin-Film Processing: All thin-film processing was performed under ambient atmosphere using room-temperature solutions and substrates unless noted otherwise. All solution concentrations refer to the total solute content. Semiconductor blends were dissolved at 1:1 weight ratio. Reference nonoriented P3HT:N2200 films were spin-coated from 1.3 wt% solutions in chlorobenzene preheated to 50 °C (140 nm thickness) and postcrystallized by annealing at 140 °C for 10 min under N_2 atmosphere. Oriented films were fabricated by doctor-blade deposition (Erichsen Coatmaster 510 stage and Zehntner ZUA 2000 applicator) at 30 °C using, typically, 50–80 µL of solution, blade height Δ = 300 µm, coating speed v = 5 mm s^{-1} and air-assisted drying (Figure S1, Supporting Information). Optimized solutions were prepared in mixtures of CF and TCB as the solvent: P3HT:N2200 at 1.3–2.1 wt% in 1:0.22 CF:TCB and P3HT:IDTBR at 3.2 wt% in 1:0.4 CF: TCB. The films were subsequently desiccated for ≈1 h to remove TCB. Oriented P3HT:IDTBR films were additionally postcrystallized by annealing at 140 °C for 10 min under N_2 atmosphere. PS backfilling overlayers were spin-coated from 4 wt% solutions in 2:1 wt/wt ethyl acetate : cyclohexanone (5000 rpm, drying time ≈5 s) to yield ≈160 nm films. PMMA backfilling overlayers were spin coated from 2 wt% solutions in acetonitrile to yield ≈60 nm films. Plasma etching was performed with the NANO instrument (Diener Electronic) operated at 900 W, 0.3 mbar working pressure and frequency of 40 kHz.

Device Fabrication: Glass substrates with prestructured ITO electrodes (180 nm, 10 Ω □$^{-1}$; Kintec Company) were cleaned by sequential sonication in acetone and isopropanol, following which 30 nm thick SnO_2 hole-blocking layers were spin-coated and annealed at 120 °C for 5 min in air. Active layer deposition, backfilling, and plasma treatment were performed as described above. Devices were completed by thermal evaporation of a 30 nm MoO_3 hole transport layer and 100 nm Ag electrode, yielding four devices (6 × 4 mm^2 area) per substrate (Figure 1c).

Characterization: Absorption spectra were recorded using a custom-built setup comprising an AvaLight-DHS-Bal light source and an AvaSpec-ULS3648 spectrometer (no correction for scattering or reflection losses). EQE and spectral responsivity analysis was performed using a 450 W Osram XBO Xenon discharge lamp as a white-light source and an Acton SP-2150i monochromator, while the photocurrent signal was measured with a Stanford Research 830 lock-in amplifier using additional amplification with a Femto DHPCA-100 amplifier. Detection speed was analyzed by recording the transient current response (Agilent DSO 6102A oscilloscope) to illumination at 520 nm modulated to give square-waves of varying frequency (Oxxius LBX520 diode laser and Agilent 33522A function generator). In all cases, polarized measurements were performed by passing the illumination light via a broadband wire-grid polarizer (WP25M-UB; Thorlabs). Unless specified otherwise, all reported device characteristics correspond to the best-performing, "hero" devices. Tensile tests on natural rubber films (thickness = 40 µm; rectangular strips ≈ 8 × 6 mm^2) were performed with an FMT-310BU force tester (Alluris) equipped with a 50 N load-cell using a constant elongation rate of 100 mm min^{-1}. Topography analysis was performed with a KLA Tencor D-500 stylus profilometer. AFM was performed with a DME DS95 Dualscope instrument in tapping mode. GIWAXS measurements were performed by means of a solid anode X-ray tube (Seimens Kristallofelx X-ray source, copper anode X-ray tube operated at 35 kV and 40 mA), Osmic confocal MaxFlux optics, X-ray beam with pinhole. The sample chamber was vacuumed to ≈1 mbar during the measurement. The incident angle (α_i) of the X-ray beam was adjusted individually for each sample in the range of 0.08°–0.12°. The scattered intensity was recorded by a 2D image plate (MAR345, marXperts GmbH, Norderstedt, Germany). The scattering vector q ($q = (4\pi/\lambda)\sin\theta$) was calibrated using a silver behenate standard. The data were processed and analyzed using Datasqueeze (University of Pennsylvania, Philadelphia, PA, USA) and OriginPro.

Supporting Information

Supporting Information is available from the Wiley Online Library or from the author.

Acknowledgements

The authors are indebted to Prof. em. Paul Smith (Swiss Federal Institute of Technology, ETH Zürich) and Peter Krebsbach and Kai Xia (KIT) for the many freely shared insights and suggestions. A.P. acknowledges

funding by the Federal Ministry of Education and Research (BMBF) and the Baden-Württemberg Ministry of Science as part of the Excellence Strategy of the German Federal and State Governments. This work was financially supported by Deutsche Forschungsgemeinschaft (DFG, German Research Foundation) through grant HE 7056/3-1.

Open Access funding enabled and organized by Projekt DEAL.

Conflict of Interest

The authors declare no conflict of interest.

Data Availability Statement

The data that support the findings of this study are available from the corresponding author upon reasonable request.

Keywords

organic photodiodes, organic semiconductors, oriented polymers, photodetectors, polarization

Received: November 4, 2021
Revised: January 27, 2022
Published online:

[1] C. Fuentes-Hernandez, W.-F. Chou, T. M. Khan, L. Diniz, J. Lukens, F. A. Larrain, V. A. Rodriguez-Toro, B. Kippelen, *Science* **2020**, *370*, 698.
[2] D. Yang, D. Ma, *Adv. Opt. Mater.* **2019**, *7*, 1800522.
[3] H. Ren, J.-D. Chen, Y.-Q. Li, J.-X. Tang, *Adv. Sci.* **2021**, *8*, 2002418.
[4] N. Strobel, N. Droseros, W. Köntges, M. Seiberlich, M. Pietsch, S. Schlisske, F. Lindheimer, R. R. Schröder, U. Lemmer, M. Pfannmöller, N. Banerji, G. Hernandez-Sosa, *Adv. Mater.* **2020**, *32*, 1908258.
[5] N. Strobel, M. Seiberlich, R. Eckstein, U. Lemmer, G. Hernandez-Sosa, *Flex. Print. Electron.* **2019**, *4*, 043001.
[6] a) C. M. Lochner, Y. Khan, A. Pierre, A. C. Arias, *Nat. Commun.* **2014**, *5*, 5745; b) A. K. Bansal, S. Hou, O. Kulyk, E. M. Bowman, I. D. W. Samuel, *Adv. Mater.* **2015**, *27*, 7638.
[7] R. Koeppe, P. Bartu, S. Bauer, N. S. Sariciftci, *Adv. Mater.* **2009**, *21*, 3510.
[8] G. Williams, C. Backhouse, H. Aziz, *Electronics* **2014**, *3*, 43.
[9] C. Vega-Colado, B. Arredondo, J. Carlos Torres, E. López-Fraguas, R. Vergaz, D. Martín-Martín, G. del Pozo, B. Romero, P. Apilo, X. Quintana, M. A. Geday, C. de Dios, J. M. Sánchez-Pena, *Sensors* **2018**, *18*, 3045.
[10] F. Snik, J. Craven-Jones, M. Escuti, S. Fineschi, D. Harrington, A. de Martino, D. Mawet, J. Riedi, J. S. Tyo, *Proc. SPIE* **2014**, *9099*, 90990B.
[11] Y. Zhao, C. Yi, S. G. Kong, Q. Pan, Y. Cheng, *Multi-Band Polarization Imaging and Applications*, Springer, Heidelberg **2016**.
[12] a) S. B. Powell, R. Garnett, J. Marshall, C. Rizk, V. Gruev, *Sci. Adv.* **2018**, *4*, eaao6841; b) N. A. Rubin, G. D'Aversa, P. Chevalier, Z. Shi, W. T. Chen, F. Capasso, *Science* **2019**, *365*, 43.
[13] a) Y. Zhou, J. Luo, Y. Zhao, C. Ge, C. Wang, L. Gao, C. Zhang, M. Hu, G. Niu, J. Tang, *Adv. Opt. Mater.* **2018**, *6*, 1800679; b) D. Wu, J. Guo, J. Du, C. Xia, L. Zeng, Y. Tian, Z. Shi, Y. Tian, X. J. Li, Y. H. Tsang, J. Jie, *ACS Nano* **2019**, *13*, 9907; c) T. Deng, S. Li, Y. Li, Y. Zhang, J. Sun, W. Yin, W. Wu, M. Zhu, Y. Wang, Z. Liu, *Nanophotonics* **2020**, *9*, 4719; d) Y. Zhao, Y. Qiu, J. Feng, J. Zhao, G. Chen, H. Gao, Y. Zhao, L. Jiang, Y. Wu, *J. Am. Chem. Soc.* **2021**, *143*, 8437.
[14] A. Falco, R. Nagel, P. Lugli, E. Bezzeccheri, R. Liguori, A. Rubino, *IEEE Sensors* **2016**, https://doi.org/10.1109/ICSENS.2016.7808585.
[15] C. Weder, C. Sarwa, C. Bastiaansen, P. Smith, *Adv. Mater.* **1997**, *9*, 1035.
[16] A. Perevedentsev, S. Aksel, K. Feldman, P. Smith, P. N. Stavrinou, D. D. C. Bradley, *J. Polym. Sci., Part B: Polym. Phys.* **2015**, *53*, 22.
[17] A. Li, D. Bilby, B. X. Dong, J. Amonoo, J. Kim, P. F. Green, *J. Polym. Sci., Part B: Polym. Phys.* **2016**, *54*, 180.
[18] D. Khim, A. Luzio, G. E. Bonacchini, G. Pace, M.-J. Lee, Y.-Y. Noh, M. Caironi, *Adv. Mater.* **2018**, *30*, 1705463.
[19] X. Shi, V. Nádaždy, A. Perevedentsev, J. M. Frost, X. Wang, E. von Hauff, R. C. I. MacKenzie, J. Nelson, *Phys. Rev. X* **2019**, *9*, 021038.
[20] N. E. Persson, S. Engmann, L. J. Richter, D. M. DeLongchamp, *Chem. Mater.* **2019**, *31*, 4133.
[21] M. Schubert, B. A. Collins, H. Mangold, I. A. Howard, W. Schindler, K. Vandewal, S. Roland, J. Behrends, F. Kraffert, R. Steyrleuthner, Z. Chen, K. Fostiropoulos, R. Bittl, A. Salleo, A. Facchetti, F. Laquai, H. W. Ade, D. Neher, *Adv. Funct. Mater.* **2014**, *24*, 4068.
[22] J. W. Jo, J. W. Jung, H. Ahn, M. J. Ko, A. K.-Y. Jen, H. J. Son, *Adv. Energy Mater.* **2017**, *7*, 1601365.
[23] N. A. Ran, S. Roland, J. A. Love, V. Savikhin, C. J. Takacs, Y.-T. Fu, H. Li, V. Coropceanu, X. Liu, J.-L. Brédas, G. C. Bazan, M. F. Toney, D. Neher, T.-Q. Nguyen, *Nat. Commun.* **2017**, *8*, 79.
[24] N. J. Cheetham, M. Ortiz, A. Perevedentsev, L.-I. Dion-Bertrand, G. M. Greetham, I. V. Sazanovich, M. Towrie, A. W. Parker, J. Nelson, C. Silva, D. D. C. Bradley, S. C. Hayes, P. N. Stavrinou, *Chem. Mater.* **2019**, *31*, 6787.
[25] M. Brinkmann, L. Hartmann, L. Biniek, K. Tremel, N. Kayunkid, *Macromol. Rapid Commun.* **2014**, *35*, 9.
[26] V. Vijayakumar, E. Zaborova, L. Biniek, H. Zeng, L. Herrmann, A. Carvalho, O. Boyron, N. Leclerc, M. Brinkmann, *ACS Appl. Mater. Interfaces* **2019**, *11*, 4942.
[27] A. Altaqui, P. Sen, H. Schrickx, J. Rech, J.-W. Lee, M. Escuti, W. You, B. J. Kim, R. Kolbas, B. T. O'Connor, M. Kudenov, *Sci. Adv.* **2021**, *7*, eabe3196.
[28] a) J. C. Wittmann, P. Smith, *Nature* **1991**, *352*, 414; b) Y. Shi, P. S. Salter, M. Li, R. A. Taylor, S. J. Elston, S. M. Morris, D. D. C. Bradley, *Adv. Funct. Mater.* **2021**, *31*, 2007493.
[29] C. Müller, M. Aghamohammadi, S. Himmelberger, P. Sonar, M. Garriga, A. Salleo, M. Campoy-Quiles, *Adv. Funct. Mater.* **2013**, *23*, 2368.
[30] B. Dörling, V. Vohra, T. T. Dao, M. Garriga, H. Murata, M. Campoy-Quiles, *J. Mater. Chem. C* **2014**, *2*, 3303.
[31] T. Rödlmeier, T. Marszalek, M. Held, S. Beck, C. Müller, R. Eckstein, A. J. Morfa, R. Lovrincic, A. Pucci, U. Lemmer, J. Zaumseil, W. Pisula, G. Hernandez-Sosa, *Chem. Mater.* **2017**, *29*, 10150.
[32] A. Perevedentsev, M. Campoy-Quiles, *Nat. Commun.* **2020**, *11*, 3610.
[33] J. Kublitski, A. Hofacker, B. K. Boroujeni, J. Benduhn, V. C. Nikolis, C. Kaiser, D. Spoltore, H. Kleemann, A. Fischer, F. Ellinger, K. Vandewal, K. Leo, *Nat. Commun.* **2021**, *12*, 551.
[34] H. Yan, B. A. Collins, E. Gann, C. Wang, H. Ade, C. R. McNeill, *ACS Nano* **2012**, *6*, 677.
[35] M. Schubert, D. Dolfen, J. Frisch, S. Roland, R. Steyrleuthner, B. Stiller, Z. Chen, U. Scherf, N. Koch, A. Facchetti, D. Neher, *Adv. Energy Mater.* **2012**, *2*, 369.
[36] R. Zhang, H. Yang, K. Zhou, J. Zhang, X. Yu, J. Liu, Y. Han, *Macromolecules* **2016**, *49*, 6987.
[37] M. Kristiansen, M. Werner, T. Tervoort, P. Smith, M. Blomenhofer, H.-W. Schmidt, *Macromolecules* **2003**, *36*, 5150.
[38] C. M. Stafford, K. E. Roskov, T. H. Epps III, M. J. Fasolka, *Rev. Sci. Instrum.* **2006**, *77*, 023908.
[39] a) X. Gu, L. Shaw, K. Gu, M. F. Toney, Z. Bao, *Nat. Commun.* **2018**, *9*, 534; b) O. Yildiz, Z. Wang, M. Borkowski, G. Fytas, P. W. M. Blom, J. J. Michels, W. Pisula, T. Marszalek, *Adv. Funct. Mater.* **2022**,

32, 2107976; c) J. J. Michels, K. Zhang, P. Wucher, P. M. Beaujuge, W. Pisula, T. Marszalek, *Nat. Mater.* **2021**, *20*, 68.
[40] F. Choffat, S. Fornera, P. Smith, W. R. Caseri, D. W. Breiby, J. W. Andreasen, M. M. Nielsen, *Adv. Funct. Mater.* **2008**, *18*, 2301.
[41] R. J. Kline, M. D. McGeehee, E. N. Kadnikova, J. Liu, J. M. J. Fréchet, M. F. Toney, *Macromolecules* **2005**, *38*, 3312.
[42] W. Huang, M. Li, F. Lin, Y. Wu, Z. Ke, X. Zhang, R. Ma, T. Yang, W. Ma, Y. Liang, *Mol. Syst. Des. Eng.* **2018**, *3*, 103.
[43] a) H. Puliyalil, U. Cvelbar, *Nanomaterials* **2016**, *6*, 108; b) M. Toma, G. Loget, R. M. Corn, *ACS Appl. Mater. Interfaces* **2014**, *6*, 11110; c) G. Q. Zhang, C. W. Lan, H. L. Bian, R. Gao, J. Zhou, *Opt. Express* **2017**, *25*, 22038.
[44] C. Neusel, G. A. Schneider, *J. Mech. Phys. Solids* **2014**, *63*, 201.
[45] J. G. A. Terlingen, A. S. Hoffman, J. Feijen, *J. Appl. Polym. Sci.* **1993**, *50*, 1529.
[46] a) G. N. Taylor, T. M. Wolf, *Polym. Eng. Sci.* **1980**, *20*, 1087; b) G. N. Taylor, T. M. Wolf, J. M. Moran, *J. Vac. Sci. Technol.* **1981**, *19*, 872.
[47] a) H. Lee, D. Lee, D. H. Sin, S. W. Kim, M. S. Jeong, K. Cho, *NPG Asia Mater.* **2018**, *10*, 469; b) S. Li, J. Li, Y. Chun, P. K. Shrestha, X. Chang, M. Pivnenko, D. Chu, *ACS Appl. Mater. Interfaces* **2021**, *13*, 19055.
[48] P. Sen, R. Yang, J. J. Rech, Y. Feng, C. H. Y. Ho, J. Huang, F. So, R. J. Kline, W. You, M. W. Kudenov, B. T. O'Connor, *Adv. Opt. Mater.* **2019**, *7*, 1801346.
[49] A. Wadsworth, *Doctoral Thesis*, Imperial College London, UK **2018**.
[50] M. Scafidi, G. Pitarresi, A. Toscano, G. Petrucci, S. Alessi, A. Ajovalasit, *Opt. Eng.* **2015**, *54*, 081206.
[51] D. Sun, T. Lu, T. Wang, *Soft Matter* **2021**, *17*, 4998.
[52] a) S. Busato, A. Perevedentsev, *Polym. Eng. Sci.* **2017**, *58*, 345; b) S. Busato, D. Kremer, A. Perevedentsev, *Macromol. Mater. Eng.* **2021**, *306*, 2100045.
[53] M. Held, A. Pichler, J. Chabeda, N. Lam, P. Hindenberg, C. Romero-Nieto, G. Hernandez-Sosa, *Adv. Sustainable Syst.* **2021**, https://doi.org/10.1002/adsu.202100035.
[54] B. Zhao, N. Tian, Y. Liu, T. Yan, W. Zhou, L. Li, Y. Zhou, G. Weng, G. Huang, *J. Polym. Sci., Part B: Polym. Phys.* **2012**, *50*, 1630.
[55] M. J. Free, V. Srisamang, J. Vail, D. Mercer, R. Kotz, D. E. Marlowe, *Contraception* **1996**, *53*, 221.